The Astrophysical Journal, 831:62 (11pp), 2016 November 1 doi:10.3847/0004-637X/831/1/62

EFFECTS OF SPIN ON HIGH-ENERGY RADIATION FROM ACCRETING BLACK HOLES

Michael O' Riordan[1], Asaf Pe'er[1], and Jonathan C. McKinney[2]
[1] Physics Department, University College Cork, Cork, Ireland; michael_oriordan@umail.ucc.ie
[2] Department of Physics and Joint Space-Science Institute, University of Maryland, College Park, MD 20742, USA
Received 2016 July 4; revised 2016 August 12; accepted 2016 August 17; published 2016 October 27

ABSTRACT

Observations of jets in X-ray binaries show a correlation between radio power and black hole spin. This correlation, if confirmed, points toward the idea that relativistic jets may be powered by the rotational energy of black holes. In order to examine this further, we perform general relativistic radiative transport calculations on magnetically arrested accretion flows, which are known to produce powerful jets via the Blandford–Znajek (BZ) mechanism. We find that the X-ray and γ-ray emission strongly depend on spin and inclination angle. Surprisingly, the high-energy power does not show the same dependence on spin as the BZ jet power, but instead can be understood as a redshift effect. In particular, photons observed perpendicular to the spin axis suffer little net redshift until originating from close to the horizon. Such observers see deeper into the hot, dense, highly magnetized inner disk region. This effect is largest for rapidly rotating black holes due to a combination of frame dragging and decreasing horizon radius. While the X-ray emission is dominated by the near horizon region, the near-infrared (NIR) radiation originates at larger radii. Therefore, the ratio of X-ray to NIR power is an observational signature of black hole spin.

Key words: accretion, accretion disks – black hole physics – radiative transfer – relativistic processes – X-rays: binaries

1. INTRODUCTION

It is widely believed that relativistic jets are powered by the rotational energy of black holes. Blandford & Znajek (1977) showed that magnetic field lines, anchored in an external accretion disk, are twisted by frame dragging in the vicinity of a rotating black hole. These field lines expand under their own pressure, transporting energy outward and accelerating any "frozen-in" plasma into jets aligned with the spin axis. Recent general relativistic magnetohydrodynamic (GRMHD) simulations of "magnetically arrested disks" (MADs; Narayan et al. 2003) showed that this process can operate with efficiencies of >100% (Tchekhovskoy et al. 2011; McKinney et al. 2012). That is, more energy flows out of the black hole than flows in, which can only be achieved by extracting rotational energy from the black hole.

Using 5 GHz radio emission from X-ray binaries (XRBs) as a proxy for jet power, Narayan & McClintock (2012) found a correlation between jet power and black hole spin (but see Fender et al. 2010; Russell et al. 2013). Their results were consistent with $P_{\rm jet} \sim a^2$, which is the scaling derived by Blandford & Znajek (1977) for slowly rotating black holes. They also found good agreement with the more accurate scaling $P_{\rm jet} \sim \Omega_H^2$ (Tchekhovskoy et al. 2010, 2012), which works up to $a \approx 0.95$. Here, a is the dimensionless spin of the black hole, $\Omega_H = a/2\,r_H$ is the angular velocity of the horizon, and $r_H = 1 + \sqrt{1 - a^2}$ is the horizon radius (we work in units where $GM = c = 1$, however, we occasionally reintroduce factors of c for clarity). If confirmed, this correlation provides observational evidence that jets are probably powered by the rotational energy of black holes.

Although it is well established that jets produce radio emission at large radii (e.g., Fender et al. 2010), the high-energy (X-ray and γ-ray) radiation could originate much closer to the black hole, and so the contribution of jets to this radiation is less certain. It has long been argued that inverse Compton emission from a corona of hot electrons surrounding the inner accretion disk can produce the observed X-ray spectrum in XRBs (e.g., Titarchuk 1994; Magdziarz & Zdziarski 1995; Esin et al. 1997, 2001; Gierlinski et al. 1997; Poutanen 1998, pp. 100–122; Cadolle Bel et al. 2006; Yuan et al. 2007; Narayan & McClintock 2008; Niedźwiecki et al. 2012, 2014; Qiao & Liu 2015). However, it is also possible that a significant fraction of the X-ray emission originates in jets (e.g., Mirabel & Rodríguez 1994; Markoff et al. 2001, 2003, 2005, 2015; Falcke et al. 2004; Bosch-Ramon et al. 2006; Gupta et al. 2006; Kaiser 2006; Kylafis et al. 2008; Maitra et al. 2009; Pe'er & Casella 2009; Pe'er & Markoff 2012; O' Riordan et al. 2016).

Near the black hole where the jet originates, it is not even necessarily easy to distinguish what one means by a disk versus a jet due to the generically low plasma β parameter and inflow-outflow regions in both the disk and jet (McKinney & Gammie 2004; McKinney 2006). Clearly, there is much uncertainty about the potentially complicated relationship between the high-energy emission, the inner regions of the disk/jet, and the central black hole. In particular, even if jets are powered by the rotational energy of black holes, due to the uncertainties in the source of the high-energy radiation, it is not clear a priori how this radiation should depend on spin.

To investigate this issue, we take fully three-dimensional GRMHD simulations with different black hole spins. We perform radiative transfer calculations with Comptonization to obtain the spectrum of radiation with a focus on high-energy radiation resolved by the region near the black hole. We restrict our attention to the low/hard state in XRBs, since it is widely accepted that jets exist during this state (with transient jets launched during state transitions; Fender et al. 2004). Interestingly, although we find a strong spin dependence for the high-energy power, this does not follow the Blandford–Znajek (BZ) scaling. Furthermore, the effects of spin are maximum for observers located perpendicular to the spin axis of the black hole. We show that the high-energy emission originates from

very close to the horizon, and the strong spin and viewing angle dependence can be understood as a redshift effect. While the X-ray power strongly depends on spin and observer inclination, the near-infrared (NIR) emission originates at larger radii and so is less sensitive to redshift effects. Therefore, for systems whose inclination angles are known, the ratio of X-ray to NIR power in the low/hard state can potentially be used to estimate spin. Since the black hole spin does not vary between the low/hard and high/soft states, this ratio would complement measurements of spin in the high/soft state (see e.g., McClintock et al. 2011, for a review).

In Section 2 we briefly describe our GRMHD simulations and radiative transport post-processing method. In Section 3 we show the dependence of radiated power on spin and calculate the effects of redshift. In Section 4 we summarize and discuss our findings.

2. MODEL

Radiatively inefficient accretion flows (RIAFs) have been used extensively to model low-luminosity systems such as the low/hard state in XRBs (see e.g., Narayan & McClintock 2008; Yuan & Narayan 2014). For RIAFs, by definition, the cooling time of a fluid element is much longer than the accretion time. Therefore, radiation is dynamically unimportant and the evolution of the disk/jet can be calculated using the non-radiative GRMHD equations. This allows a separation between the dynamical simulations and radiative transport post-processing of the simulation results. We use the HARM code (Gammie et al. 2003), which solves the GRMHD equations using a conservative, shock-capturing scheme.

For our purposes, we choose five MAD accretion flows with spins $a = \{0.1, 0.2, 0.5, 0.9, 0.99\}$ (these are A0.1N100, A0.2N100, A0.5N100, A0.9N100, and A0.99N100 from McKinney et al. 2012). In these models, the black hole magnetosphere compresses the inner accretion disk such that it becomes geometrically thin and the magneto-rotational instability is suppressed. These MAD models efficiently extract rotational energy from the black hole via the BZ mechanism, launching jets along the spin axis (Tchekhovskoy et al. 2011; McKinney et al. 2012). Estimates of the jet power, based on integrating fluid energy fluxes (dominated by the Poynting flux), show that the power scales are as expected for the BZ mechanism (with corrections for high spins and disk thickness; Tchekhovskoy et al. 2012). However, such estimates are based solely on the dynamical properties of the fluid, so the radiated power must be calculated in order to compare with observations.

Since we limit our analysis to the low/hard state in XRBs, we choose a black hole mass of $10M_\odot$, and accretion rate of $\dot{M} = 10^{-5}\dot{M}_{\rm Edd}$. Such a low accretion rate ensures that the flow is radiatively inefficient (see e.g., Narayan & McClintock 2008). The Eddington accretion rate, $\dot{M}_{\rm Edd}$, is defined to be the mass accretion rate at which a disk with radiative efficiency 0.1 would radiate at the Eddington luminosity $L_{\rm Edd}$. That is, $\dot{M}_{\rm Edd}\, c^2 = 10\, L_{\rm Edd}$ (Narayan & McClintock 2008). Although radio emission is expected to originate in the jet at large radii, computational limitations force us to restrict our analysis to the inner $r \approx 200\, r_g$, where $r_g = GM/c^2$ is the gravitational radius. While the setup we use cannot properly capture radio emission, the NIR to high-energy emission ($\nu \gtrsim 10^{13}$ Hz) is dominated by regions close to the black hole, and so setting the boundary to $r = 200\, r_g$ has little effect on our results at these frequencies.

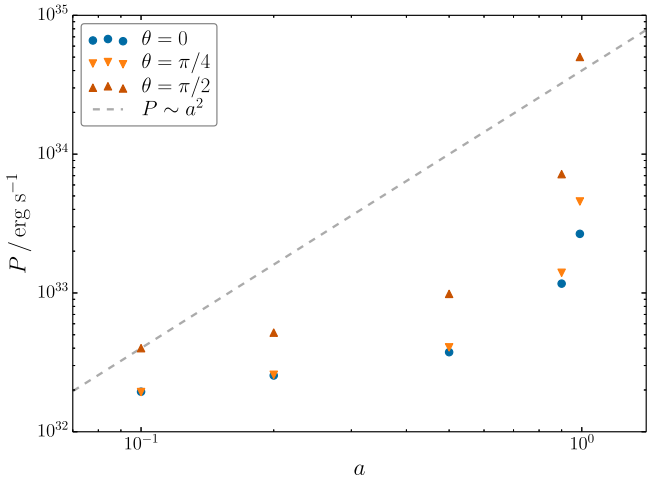

Figure 1. Integrated power vs. spin for observer viewing angles of $\theta = 0$ (parallel to the spin axis), $\theta = \pi/4$, and $\theta = \pi/2$ (perpendicular to the spin axis). The dashed line corresponds to the BZ scaling $P \sim a^2$. The dependence of the radiated power on spin clearly deviates significantly from this scaling. Interestingly, the effects of spin are strongest for observers located perpendicular to the spin axis, with a difference of more than two orders of magnitude in power between the $a = 0.1$ and $a = 0.99$ cases.

As discussed in O' Riordan et al. (2016), the center of the highly magnetized, low-density funnel can become artificially dense and hot due to the introduction of numerical density floors. We, therefore, remove this floor material by setting the density to zero in regions where $b^2/\rho > \zeta$. Here, ρ is the rest mass density, and $b^2 = b^\mu b_\mu$, where b^μ is the magnetic 4-field. The magnetic 4-field can be written in terms of the 3-field B^i as $b^\mu = h^\mu_\nu\, B^\nu/u^t$, where $h^\mu_\nu = \delta^\mu_\nu + u^\mu u_\nu$ is a projection tensor, u^μ is the fluid 4-velocity, and $B^0 = 0$. We choose $\zeta = 20$ at the horizon, and linearly interpolate to $\zeta = 10$ at $r = 10$. For $r > 10$, we simply set $\zeta = 10$. This interpolation happens to ensure that the injected floor material is accurately removed, without unnecessarily removing material very close to the black hole, which can naturally become highly magnetized.

We calculate spectra using the same general relativistic radiative transport code as in O' Riordan et al. (2016), which is based on the freely available grmonty (Dolence et al. 2009). This code uses the fluid data as input, and calculates the spectra assuming synchrotron emission, self-absorption, and Compton scattering from a Maxwell–Jüttner distribution of electrons. We assume a constant proton-to-electron temperature ratio T_p/T_e. However, since differences in density and magnetization in the disk and jet can lead to different cooling rates for the electrons (Foucart et al. 2016; Ressler et al. 2015), we allow this temperature ratio to vary independently in these regions. In our models, the X-rays are dominated by the highly magnetized inner disk (which is nearly indistinguishable from the jet base) and so varying T_p/T_e independently in the disk and jet has a negligible effect on the high-energy radiation in this case. Therefore, we simply choose a constant ratio of $T_p/T_e = 30$ everywhere (we find the same dependence of the radiated power on spin with $T_p/T_e = 3$ and $T_p/T_e = 10$).

3. RESULTS

3.1. Radiated Power

In Figure 1 we show the time-averaged radiated power (frequency integrated between 10^{13} and 10^{24} Hz) for different

spins and viewing angles. In what follows, any time averaging corresponds to the quasi-steady state between $t = 10{,}000\, r_g/c$ and $t = 14{,}000\, r_g/c$, with steps of $\Delta t = 400\, r_g/c$. We investigated the stability of this averaging in the extreme case of $a = 0.99$. First, we doubled our time resolution between $t = 10{,}000\, r_g/c$ and $t = 14{,}000\, r_g/c$. We also increased our averaging window to $t = 18{,}000\, r_g/c$, and found identical results in all cases.

For observers located parallel to the spin axis ($\theta = 0$), there is a difference of approximately one order of magnitude between the $a = 0.1$ and $a = 0.99$ cases. This difference increases to more than two orders of magnitude for observers perpendicular to the spin axis. Interestingly, the dependence of the radiated power on spin is significantly different from the BZ scaling. As shown below, the origin of this discrepancy is that the emission in our MAD models is dominated by the inner disk, very close to the black hole horizon. The strong dependence on spin and viewing angles can be understood as a somewhat surprising redshift effect.

For any fluid quantity Q, we define the density-weighted, shell-average $\langle Q \rangle_\rho$ to be

$$\langle Q \rangle_\rho = \frac{\int dA\ \rho\ Q}{\int dA\ \rho}, \tag{1}$$

where $dA = \sqrt{-g}\ dx^\theta dx^\phi$, and $g = \det(g_{\mu\nu})$ are the metric determinant. In all our models, the Compton y parameter is $y \lesssim 1$, and so, to a good approximation, we can show the effects of spin on the power by treating synchrotron emission alone. For a thermal electron distribution, the (comoving) synchrotron power scales as $P_{\rm syn} \sim \int dV n B^2 \Theta^2$, where $dV = \sqrt{-g}\ dx^r dx^\theta dx^\phi$, n is the electron number density, B is the magnetic field strength, and $\Theta = kT_e/mc^2$ is the dimensionless electron temperature. In Figure 2 we show the time-averaged $\langle nB^2\Theta^2 \rangle_\rho$, which is proportional to the synchrotron emissivity νj_ν (where j_ν has units of erg cm^{-3} s^{-1} ster^{-1} Hz^{-1}; Rybicki & Lightman 1979).

Clearly, the emissivity is a strong function of r, and increases toward the black hole due to the increase in magnetic energy density and compression by the magnetosphere. Furthermore, the emissivity profiles are roughly independent of spin. This is likely a consequence of the MAD state. McKinney et al. (2012), Tchekhovskoy et al. (2012) showed that in MAD accretion flows the magnetic flux saturates near the horizon, depending only weakly on spin (∼20% difference between the $a = 0$ and $a = 1$ simulations). Therefore, for a fixed disk angular thickness, black hole mass and accretion rate, we expect the profile of B^2 to be the same for different spins. Close to the black hole, the fluid properties are determined by an approximate force balance between the inner magnetosphere and the thermal and ram pressures (McKinney et al. 2012), and so this explains why the fluid properties are also roughly independent of spin.

The bottom panel shows the (comoving) synchrotron power $P_{\rm syn}(r) \sim \int_{r_H}^{r} dV n B^2 \Theta^2$. It is clear from this plot that the radiated power is dominated by the near horizon region. The synchrotron emissivity profiles are independent of spin, and so the increase in power is simply a consequence of the decreasing horizon radius (from $r = 2\, r_g$ to $r = 1\, r_g$ as the spin increases from $a = 0$ to $a = 1$). However, since the difference in power is due to radiation from $r \lesssim 2\, r_g$, it will be strongly

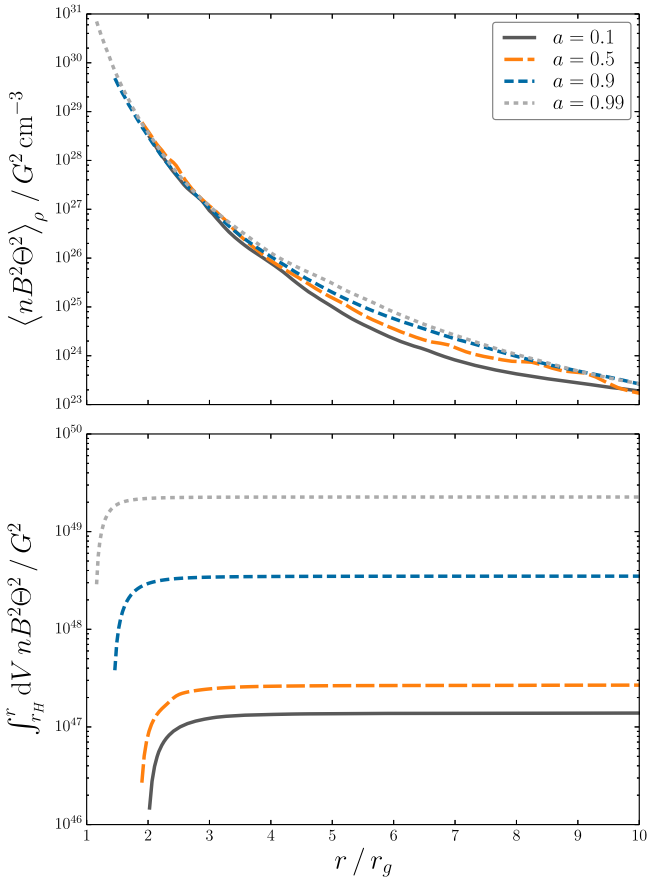

Figure 2. Time- and shell-averaged $nB^2\Theta^2$, weighted by the density. This quantity is proportional to the total synchrotron emissivity. The bottom panel shows $nB^2\Theta^2$ integrated over volume with the integral taken between the horizon and r. This quantity is proportional to the total synchrotron power. It is clear that the (comoving) radiated power is dominated by the near horizon region.

gravitationally redshifted and so it is not immediately obvious that this effect is observable. In order to check that this is in fact the reason for the spin dependence in Figure 1, we must estimate the observed power. That is, we must account for the effects of redshift (both gravitational and Doppler).

Interestingly, as we explain in Section 3.2, redshift effects naturally explain the dependence on spin and viewing angle. In particular, for rapidly rotating black holes, frame dragging ensures that photons received by observers located at $\theta = \pi/2$ suffer little net redshift until very close to the horizon. In this case, there is little difference between the comoving and observed power, and so these observers see a very large increase in radiated power with spin. Although this effect is largest for observers perpendicular to the spin axis, observers located parallel to the spin axis should also see an increase in power due to the fact that the radius of the event horizon (i.e., the infinite redshift surface) decreases with spin.

3.2. Redshift

We consider the Kerr spacetime with metric $g_{\mu\nu}$ in Boyer–Lindquist coordinates. We define the redshift factor to be the ratio of the energy at infinity to the energy in the rest frame of

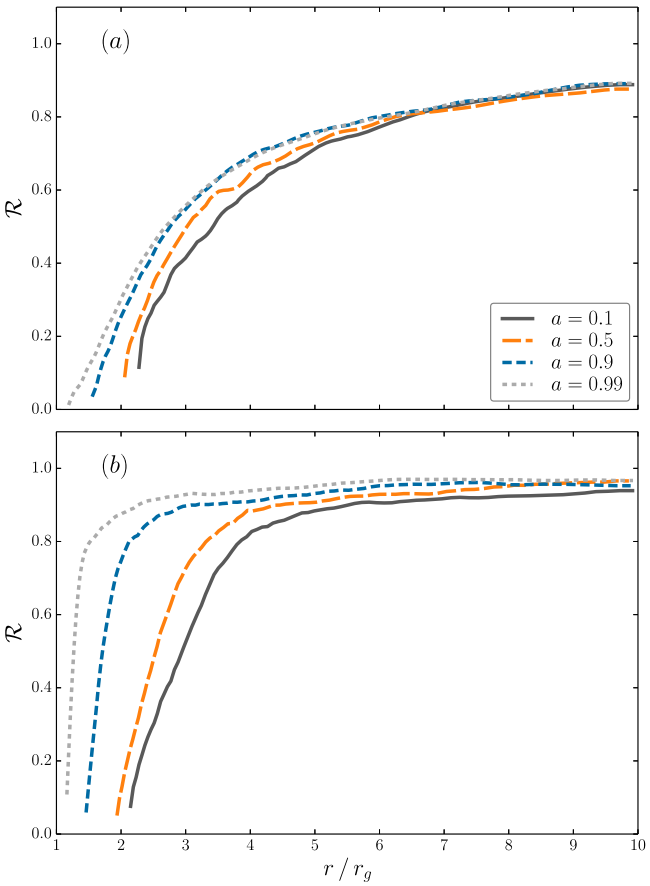

Figure 3. Redshifts for different spins and viewing angles (a): $\theta = 0$, (b): $\theta = \pi/2$. These were calculated numerically from snapshots of the GRMHD data. The redshift profiles are much flatter for observers with $\theta = \pi/2$. That is, photons received by these observers suffer little net redshift until very close to the horizon. Observers with $\theta = \pi/2$ see much deeper into the inner disk than observers with $\theta = 0$.

the fluid

$$\mathcal{R} = \frac{E_\infty}{E} = \frac{\xi^\mu p_\mu}{u^\mu p_\mu} = \frac{p_t}{u^\mu p_\mu}. \quad (2)$$

Here, u^μ is the fluid 4-velocity, p^μ is the photon 4-momentum, and $\xi^\mu = \delta^\mu_t$ is the Killing vector associated with stationarity. Since p_t is conserved along geodesics, all the above quantities can be measured at the location of the emitting fluid element.

In Figure 3, we show the numerically calculated redshift profiles for different spins and viewing angles. For a given spin and viewing angle, this calculation shows the average redshift experienced by a photon as a function of r. The top panel shows the redshift factor for an observer with $\theta = 0$. Close to the black hole, the θ velocity is negligible and so Doppler boosting is unimportant for these observers. Therefore, for $a = 0.1$, the redshift factor is almost identical to the Schwarzschild case. More accurately, for observers located at $\theta = 0$, the redshift is given by the lapse function $\alpha = \sqrt{-g_{tt} + \Omega^2 g_{\phi\phi}}$, where $\Omega = -g_{t\phi}/g_{\phi\phi}$ is the angular velocity of a "zero angular momentum observer" (ZAMO; Bardeen et al. 1972; MacDonald & Thorne 1982). Note, however, that $\mathcal{R} = \alpha$ only if $\chi^\mu p_\mu = p_\phi = 0$, where $\chi^\mu = \delta^\mu_\phi$ is the Killing vector associated with axisymmetry (see Appendix A for details). Importantly, although these profiles are identical at large radii, they deviate from each other close to the black hole, since the horizon radius decreases with spin.

The bottom panel shows the redshift factor for observers with $\theta = \pi/2$. These profiles are strikingly different from the $\theta = 0$ case. In particular, due to a combination of frame dragging and Doppler boosting, photons suffer little net redshift until very close to the horizon. Observers located at $\theta = \pi/2$ see deeper into regions of higher emissivity. This naturally explains the large difference in observed power between the $\theta = 0$ and $\theta = \pi/2$ inclinations.

While these calculations use model-dependent fluid data as input, we show in Appendix A that the flattening of the redshift profile with spin is in fact a very general feature of rotating black holes. That is, the redshift profiles depend only weakly on the details of the accretion model, with the main contributions being black hole spin and observer viewing angle. Therefore, for systems in which the comoving power is dominated by fluid close to the horizon, we expect the high-energy emission to be a robust signature of spin and viewing angle.

3.3. Spectra and Observational Signatures of Black Hole Spin

In Figure 4 we show spectra for different spins and viewing angles, calculated from snapshots of the fluid data. In the top panel, we show spectra for observers with $\theta = \pi/2$, which maximizes the effects of spin. For the $a = 0.1$ case, the synchrotron emission peaks in the optical, while for the $a = 0.99$ case this peak increases to the X-rays. There is also clear γ-ray emission due to inverse Compton scattering, which becomes more pronounced with increasing spin. Interestingly, the NIR emission is roughly constant with spin, while the high-energy radiation, namely the X-rays and γ-rays, vary significantly with spin. The bottom panel shows the effects of varying observer inclination in the $a = 0.9$ case. Both the total luminosity and frequency of the peak emission increase with viewing angle. Interestingly, there is little difference between the $\theta = 0$ and $\theta = \pi/4$ inclinations (see also Figure 1). However, the luminosity increases by roughly an order of magnitude between the $\theta = \pi/4$ and $\theta = \pi/2$ cases.

As with the total radiated power, the dependence of the spectra on spin and viewing angle can be understood as a simple consequence of the emission radius. In Figure 5 we show $\langle B\Theta^2 \rangle_\rho$ as a function of radius and spin. This quantity is proportional to the characteristic synchrotron frequency and so, as with the total radiated power, we expect the frequency of emission to increase toward the horizon. For higher spins and inclinations, observers receive radiation from smaller radii and, therefore, higher frequencies. Lower-frequency photons come from larger radii and so are less sensitive to redshift effects. Therefore, the low-frequency power should vary less with spin and viewing angle. Furthermore, since the emission is dominated by the near horizon region, we expect the light curves to show significant variability over short timescales ($\sim$few r_g/c). We also expect the high-frequency emission to vary over shorter timescales than the low-frequency emission, with a factor of $\sim$few difference between the NIR and X-ray variability timescales.

In Figure 6 we show the (time-averaged) ratio of the X-ray (integrated between 10^{16} and 10^{19} Hz) to NIR (integrated between 10^{13} and 10^{14} Hz) power. As expected, this ratio depends very strongly on viewing angle and spin. Therefore, for systems whose inclination angle is known, especially those

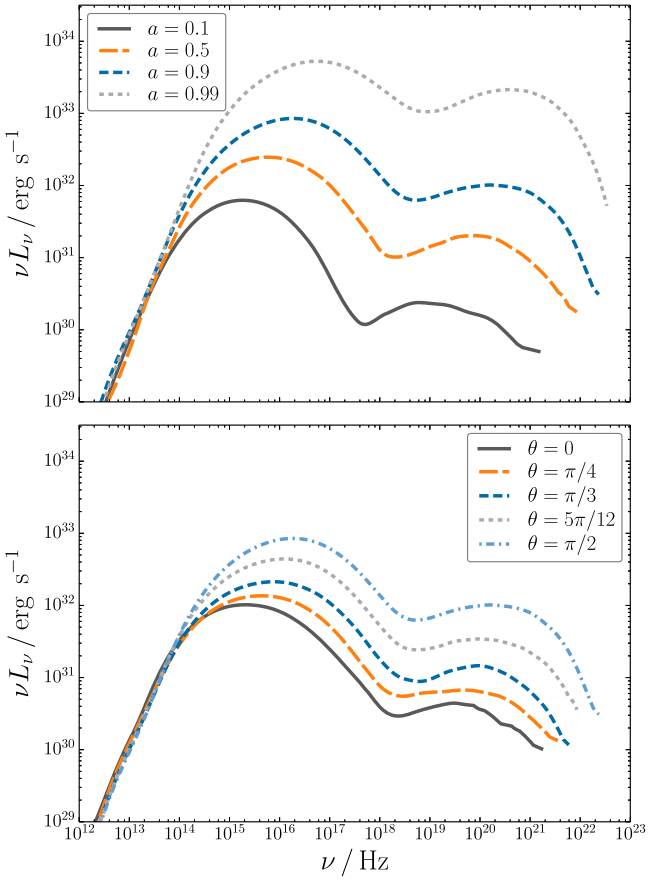

Figure 4. The top panel shows spectra for observers with $\theta = \pi/2$, calculated from snapshots of the fluid data. The NIR emission is roughly constant with spin while the X-rays and γ-rays vary significantly. The bottom panel shows the dependence on viewing angle for the $a = 0.9$ case. Both the luminosity and frequency of emission increase with viewing angle.

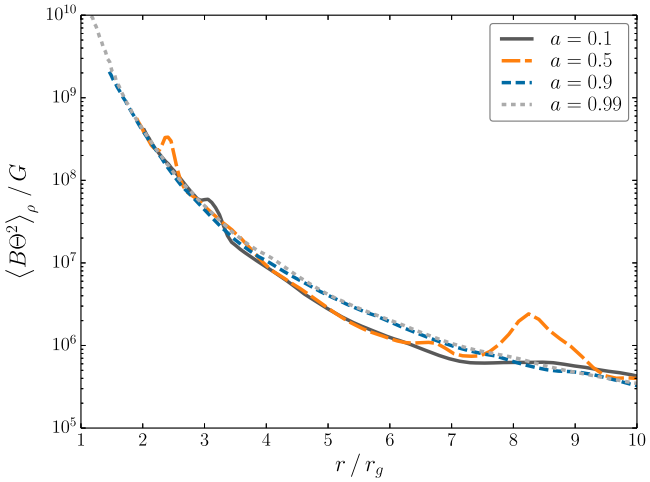

Figure 5. Time- and shell-averaged $B\Theta^2$, weighted by the density. This quantity is proportional to the characteristic synchrotron frequency. The high-energy emission is dominated by the near horizon region.

with large inclinations, the ratio $P_X/P_{\rm NIR}$ is a strong signature of spin. The black hole spin likely does not vary significantly between the low/hard and high/soft states, and so this ratio potentially compliments measurements of spin in the high/soft state. Since the synchrotron frequency depends reasonably

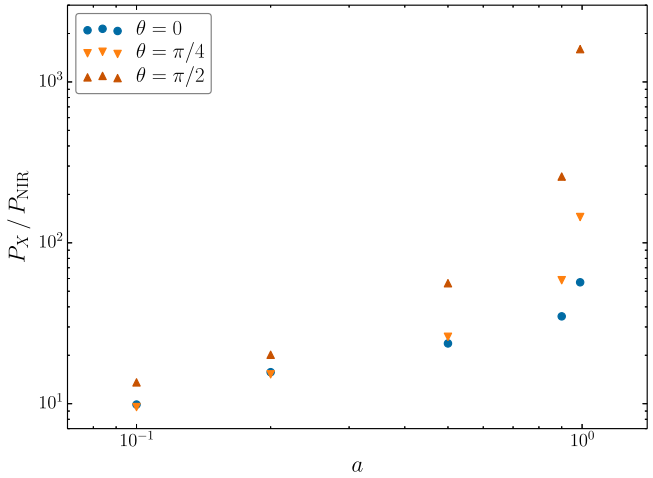

Figure 6. Ratio of the X-ray power to the NIR power for different spins and viewing angles. For large inclinations, this ratio depends very strongly on spin.

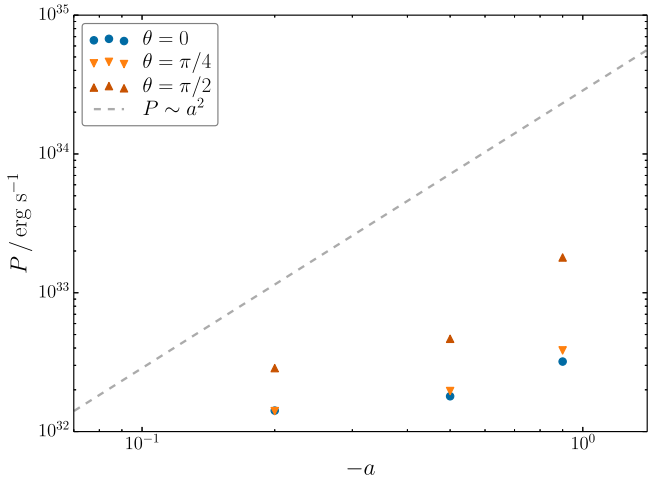

Figure 7. Integrated power vs. spin for retrograde spins. The total radiated power is lower in the retrograde case than the prograde case due to a combination of redshift and the fact that less magnetic flux is trapped in the retrograde case.

weakly on our choice of mass accretion rate ($\nu_{\rm syn} \sim \dot{M}^{1/2}$; see Appendix B), we expect this ratio to be a robust signature over a range of accretion rates.

3.4. Retrograde Spin

For comparison with Figure 1, in Figure 7 we show the integrated power versus spin for retrograde spins $a = \{-0.2, -0.5, -0.9\}$. As in the prograde case, the radiated power increases with spin and this effect is largest for observers perpendicular to the spin axis. Interestingly, the total radiated power is lower in the retrograde case than in the prograde case. This is likely due to the fact that prograde black holes trap more magnetic flux close to the horizon than retrograde black holes (Tchekhovskoy & McKinney 2012). Our results show a difference of a factor of ~3 between the $a = -0.9$ and $a = 0.9$ cases, which is consistent with the findings of Tchekhovskoy & McKinney (2012). Importantly, although the radiated power is not completely symmetric with spin, there is clearly a degeneracy between the prograde and retrograde cases. Therefore, while the ratio of the X-ray to NIR power discussed in

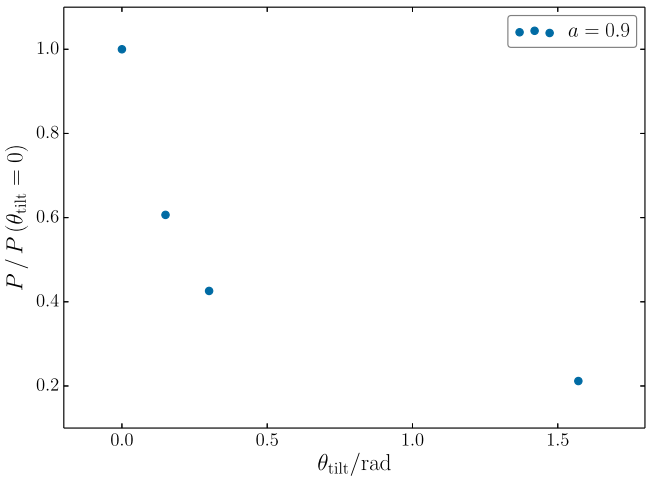

Figure 8. Observed integrated power (as a fraction of untilted power) vs. relative tilt angle. Since the emission is dominated by the near horizon region, for small misalignments there is little deviation from the untilted case.

Section 3.3 is an observational probe of spin, more information would be required to distinguish between prograde and retrograde spins.

3.5. Misalignment between Jet/Disk and Spin Axis

In the models considered so far, the disk angular momentum axis is aligned perpendicular to the black hole spin axis, while the jet points along the spin axis. In principle, however, the accreting plasma can have an arbitrary angular momentum axis. McKinney et al. (2013) studied systems in which there is a misalignment between the disk/jet and the black hole spin axis. They reported a "magneto-spin alignment" mechanism which tends to align disks and jets with the rotation axis at small radii. Therefore, since the emission in our models is dominated by the near horizon region, we expect our results to be robust to minor misalignments.

In Figure 8 we show the integrated power versus relative tilt angle for the $a = 0.9$ case, with the observer located perpendicular to the spin axis. The relative tilt angle, $\theta_{\rm tilt}$, is defined to be the angle between the spin axis and the disk's angular momentum axis at large distances. The tilt angles (in radians) are $\theta_{\rm tilt} = \{0.0, 0.15, 0.3, \pi/2\}$. There is a factor ~2.5 difference in the observed power between the untilted and $\theta_{\rm tilt} = 0.3$ rad cases, and a difference of ~5 between the untilted and fully tilted ($\theta_{\rm tilt} = \pi/2$ rad) cases. We also considered a small tilt of $\theta_{\rm tilt} = 0.15$ rad for the extreme case of $a = 0.99$, and found a difference of <2 between the untilted and tilted models. Therefore, we expect our results to be valid for systems with minor misalignments between the disk/jet and the black hole spin axis.

4. SUMMARY AND DISCUSSION

In this work, we calculated the effects of spin on high-energy emission from the low/hard state in XRBs. We modeled the low/hard state as a MAD accretion flow, and investigated both prograde and retrograde spins. We found that the X-ray power strongly depends on spin and observer inclination. In particular, the spin dependence is strikingly different from the BZ dependence expected for jet emission. In our models, the X-rays are dominated by the inner disk, and the strong dependence on spin and viewing angle can be understood as a redshift effect. For high spins and inclination angles, observers receive photons from smaller radii and, therefore, regions of larger synchrotron emissivity. Since the high-energy emission originates close to the horizon, it is more sensitive to spin than the low-energy emission that originates from larger radii. We identified the ratio of the X-ray power to NIR power as an observational signature of spin. This quantity could potentially be used to estimate spin, and would complement measurements of spin based on observations in the high/soft state.

While we expect this ratio to be particularly useful in systems with large inclinations, in general, its dependence on quantities such as the viewing angle introduces significant degeneracy. Therefore, by itself, this ratio cannot uniquely determine the black hole spin. However, since the high-energy spectrum in the low/hard state is clearly sensitive to both spin and viewing angle, it may be possible to use more features of the spectrum to constrain these quantities. In particular, following the approach of the continuum-fitting (CF) and Fe line methods (e.g., McClintock et al. 2011), one could build up models of high-energy spectra for different spins and inclinations and, for a given observational spectrum, find the best χ^2 fit. This new approach could potentially cross-validate existing methods based on fitting observations in the high/soft state. A disadvantage of this method is that it cannot easily distinguish between prograde and retrograde spins. Both the CF and Fe line methods use the ISCO, which is monotonic with spin. The method described here relies on the horizon radius and the effects of redshift and so is more symmetric with spin. Therefore, more information would be needed to break the degeneracy between retrograde and prograde spins.

The dependence of the high-energy power on spin is due to the combination of two main components, the redshift and synchrotron emissivity profiles. Interestingly, the behavior of the redshift is in fact a very general feature of rotating black holes, and is largely independent of the details of accretion. On the other hand, the emissivity itself is a model-dependent quantity. Our results rely on the fact that the comoving synchrotron power in our MAD models is strongly dominated by the near horizon region. The observed high-energy radiation should, therefore, be highly variable on timescales in the order of a few light-crossing times. Furthermore, we expect the variability timescale for the lower-frequency emission to be longer, since this originates at larger radii.

The spectra shown in Figure 4 are consistent with the basic observed X-ray hardness/flux relations for XRBs in the low/hard state (Fender et al. 2004). The time-averaged X-ray hardness ratio (defined to be the ratio of the flux at 6.3–10.5 keV to the flux at 3.8–7.3 keV; Fender et al. 2004; Belloni et al. 2005) varies between 0.7 and 0.9, with higher spins slightly softer than lower spins. The luminosities in the low spin cases are likely somewhat lower than expected for the low/hard state, and are probably more consistent with the so-called quiescent state (e.g., Remillard & McClintock 2006). However, this is not a serious issue. As shown in Appendix B, small changes in the accretion rate can significantly increase the total luminosity without greatly affecting the frequency of emission. Therefore, increasing the luminosity would not change our conclusions regarding the scaling in Figure 1 or the ratio $P_X/P_{\rm NIR}$ in Figure 6.

Mościbrodzka et al. (2009) considered the effects of spin and viewing angle on radiation from nonMAD (called SANE in Narayan et al. 2012) accretion flows in the context of Sgr A*. Interestingly, while they found that the X-ray flux increases dramatically with both spin and observer inclination, they attribute this dependence to a different effect than the one described here. In their models, the X-ray emission is produced by scattering from hot electrons at $r = r_{\rm ISCO}$, and so the dependence on spin manifests itself in a very similar manner to thin disks (see e.g., McClintock et al. 2011). In our models, by contrast, most of the observed high-energy radiation originates from right outside the horizon, with the ISCO playing no special role. This can likely be attributed to the fact that the disks considered here are geometrically thicker, and so the density does not drop off significantly inside the ISCO. Therefore, the our results are probably more relevant for low-luminosity, radiatively inefficient systems, in which the disk is expected to be geometrically thick.

Furthermore, our work improves upon this study in two major areas. First, our simulations are fully 3D, which is required to avoid decaying turbulence and reach a well defined steady state (Cowling 1933; Sądowski et al. 2015). Axisymmetric simulations cannot reliably capture the effects of spin, since the resulting radiation will be influenced by the extent to which the spin has affected the flow by the time the turbulence decays. Second, in MAD models, the final amount of magnetic flux at the horizon is independent of the initial flux content of the torus, which in SANE models can artificially introduce a spin dependence (Tchekhovskoy & McKinney 2012; Tchekhovskoy et al. 2012). Therefore, MAD models are more reliable for studying the effects of spin on the high-energy radiation.

While our calculations apply to MAD accretion flows in the low/hard state, the redshift effects described here might also be important when considering thin MADs in the high/soft state. Avara et al. (2016) demonstrated an 80% deviation from the standard Novikov–Thorne radiative efficiency, with most of the radiation coming from at or below the ISCO. As shown here, for rapidly spinning black holes, radiation from small radii is very strongly affected by variations in spin and viewing angle. Therefore, if the radiation from thin MADs originates at smaller radii than expected for standard thin disks, this could have important implications for measurements of spin in the high/soft state.

Our analysis was carried out for a black hole mass of $M = 10M_\odot$. However, since the relevant length and timescales are set by M, we can scale our results to arbitrary masses as follows. Assuming that the accretion rate is a fixed fraction of the Eddington rate $\dot{M} \sim \dot{M}_{\rm Edd} \sim M$, from Appendix B we find that $n \sim M^{-1}$, $B \sim M^{-1/2}$, and $\Theta \sim M^0$. These relationships can be used to scale the spectral features in Figure 4 to supermassive black holes. Importantly, however, this scaling is only appropriate for systems that are well described by RIAFs. Therefore, our results are potentially relevant for accreting supermassive black hole systems such as Sgr A* and low-luminosity subclasses of active galactic nucleus such as LINERS and BL Lac objects (see e.g., Yuan & Narayan 2014). Although BL Lacs (and blazars in general) have jets roughly aligned with the observer, at small radii there could be a misalignment between the jet and spin axes (see Section 3.5). Such a misalignment could significantly enhance the high-energy emission from close to the black hole, leading to the intriguing possibility that near horizon emission is responsible for the short-timescale variability observed in these systems (e.g., Aharonian et al. 2007; Albert et al. 2007; Aleksić et al. 2011; Ackermann et al. 2016).

The current work is somewhat limited by the assumption of a thermal distribution of electrons. The highly magnetized inner disk region could contain a significant number of non-thermal particles due to acceleration by magnetic reconnection (e.g., Sironi & Spitkovsky 2014). However, thermal electrons might dominate emission from near the horizon, which has been sufficient to explain the low-hard-like state in Sgr A* and M87 (Dexter et al. 2012; Broderick et al. 2014; Broderick & Tchekhovskoy 2015). Furthermore, different prescriptions for treating the electron temperature might reduce the dominance of emission from the inner disk and instead "light up" the funnel wall region (e.g., Mościbrodzka & Falcke 2013; Mościbrodzka et al. 2014). These prescriptions usually separate the jet and disk based on b^2/ρ or the plasma β. In our models, the inner disk is highly magnetized and so differentiating between the jet and disk based on the magnetization alone would in fact treat the inner disk region in a similar manner to the jet. The treatment of the electron physics in accretion disks and jets remains an active area of research, and we will apply our results with new models of electron physics as they become available.

The authors would like to thank the anonymous referee for helpful suggestions that have improved the quality of the manuscript. J.C.M. would like to thank Alexander Tchekhovskoy for providing simulation data. MOR is supported by the Irish Research Council under grant number GOIPG/2013/315. This research was partially supported by the European Union Seventh Framework Programme (FP7/2007-2013) under grant agreement No. 618499. J.C.M. acknowledges NASA/NSF/TCAN (NNX14AB46G), NSF/XSEDE/TACC (TGPHY120005), and NASA/Pleiades (SMD-14-5451).

APPENDIX A
EFFECTS OF SPIN ON THE REDSHIFT PROFILES

A.1. Analytic Expression for the Redshift Factor

To understand the dependence of the redshift factor on spin, we focus on the simple case of circular motion in the r–ϕ plane. In what follows, we denote quantities in the coordinate (lab) frame with no primes on the index, in the orthonormal "ZAMO" frame with one prime, and in the orthonormal fluid frame with two primes. The Killing vectors associated with stationarity and axisymmetry are $\xi^\mu = \delta^\mu_t$, and $\chi^\mu = \delta^\mu_\phi$. For circular motion, the 4-velocity can be written as $u^\mu = u^t(\xi^\mu + v^\phi \chi^\mu)$, where $v^\phi = u^\phi/u^t$. The condition that the 4-velocity be timelike, $g_{\mu\nu}u^\mu u^\nu = -1$, gives

$$u^t = (-g_{tt} - 2g_{t\phi}v^\phi - g_{\phi\phi}(v^\phi)^2)^{-1/2}. \quad (3)$$

Defining $\mathcal{P}_i = p_i/p_t$, we can write the redshift for circular motion as (Cunningham & Bardeen 1972, 1973; Fanton et al. 1997)

$$\mathcal{R} = \frac{1}{u^t(1 + v^\phi \mathcal{P}_\phi)}. \quad (4)$$

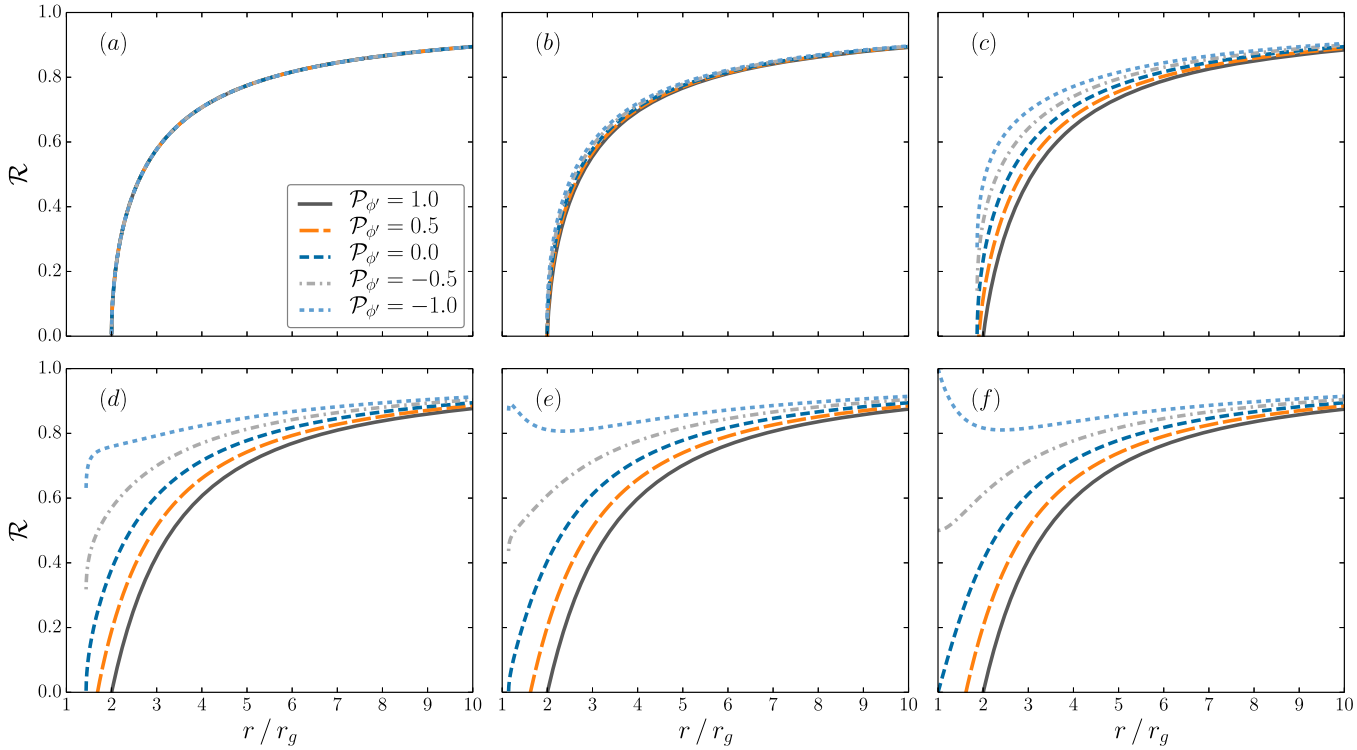

Figure 9. Redshifts for a source with $v^{\phi} = \Omega$ (Equation (13)). (a): $a = 0.1$, (b): $a = 0.2$, (c): $a = 0.5$, (d): $a = 0.9$. (e): $a = 0.99$, (f): $a = 1.0$. For high spins, photons emitted in the ϕ direction in the ZAMO frame suffer little redshift until very close to the horizon.

The photon 4-momentum is a null vector and so, in the fluid frame, we have

$$\mathcal{P}^2_{r''} + \mathcal{P}^2_{\theta''} + \mathcal{P}^2_{\phi''} = 1. \tag{5}$$

Therefore, $\mathcal{P}_{\phi''}$ is bounded by ± 1, corresponding to photons emitted in the $\mp\phi$ directions. The ZAMO and fluid frames are simply related by a Lorentz transformation, and so

$$\mathcal{P}_{\phi'} = \frac{\mathcal{P}_{\phi''} - v^{\phi'}}{1 - v^{\phi'}\,\mathcal{P}_{\phi''}}. \tag{6}$$

The transformations from the Boyer–Lindquist coordinate basis to the orthonormal ZAMO basis are given by Bardeen et al. (1972)

$$e_{\nu'} = e^{\mu}{}_{\nu'}\,\partial_{\mu}, \qquad e^{\nu'} = e_{\mu}{}^{\nu'} dx^{\mu}. \tag{7}$$

The only non-zero components are

$$e^{t}{}_{t'} = 1/\alpha,\ e^{r}{}_{r'} = 1/\sqrt{g_{rr}},\ e^{\theta}{}_{\theta'} = 1/\sqrt{g_{\theta\theta}},$$
$$e^{\phi}{}_{\phi'} = 1/\sqrt{g_{\phi\phi}},\ e^{\phi}{}_{t'} = \Omega/\alpha \tag{8}$$

$$e_{t}{}^{t'} = \alpha,\ e_{r}{}^{r'} = \sqrt{g_{rr}},\ e_{\theta}{}^{\theta'} = \sqrt{g_{\theta\theta}},$$
$$e_{\phi}{}^{\phi'} = \sqrt{g_{\phi\phi}},\ e_{t}{}^{\phi'} = -\Omega\sqrt{g_{\phi\phi}}, \tag{9}$$

where

$$\Omega = -\frac{g_{t\phi}}{g_{\phi\phi}}, \qquad \alpha = \sqrt{-g_{tt} + \Omega^2 g_{\phi\phi}}. \tag{10}$$

Transforming from the ZAMO frame to the coordinate frame gives

$$\mathcal{P}_{\phi} = \frac{\sqrt{g_{\phi\phi}}\,\mathcal{P}_{\phi'}}{\alpha - \Omega\sqrt{g_{\phi\phi}}\,\mathcal{P}_{\phi'}}, \tag{11}$$

$$v^{\phi} = \frac{\alpha}{\sqrt{g_{\phi\phi}}}\,v^{\phi'} + \Omega. \tag{12}$$

Finally, the redshift for circular motion is given by Equation (4), with $\mathcal{P}_{\phi}$ related to the fluid frame $\mathcal{P}_{\phi''}$ by Equations (6) and (11), and v^{ϕ} related to the ZAMO frame $v^{\phi'}$ by Equation (12).

In the special case of a source with zero angular momentum, $v^{\phi'} = 0 \Rightarrow v^{\phi} = \Omega$, and equation 4 becomes

$$\mathcal{R} = \alpha - \Omega\sqrt{g_{\phi\phi}}\,\mathcal{P}_{\phi'}, \tag{13}$$

which is simply the transformation $p_t = e_t{}^{\nu'}\,p_{\nu'}$. In Figure 9 we show the redshift for a ZAMO (Equation (13)), as a function of $\mathcal{P}_{\phi'}$, for different spins. For high spins, photons emitted in the ϕ direction (those with $\mathcal{P}_{\phi'} = -1$) suffer little redshift until right outside the horizon. In fact, for a maximally spinning black hole, $\mathcal{R} \to 1$ as $r \to r_H$. On average, observers with $\theta = \pi/2$ receive photons with larger ϕ momentum than observers located at $\theta = 0$. Therefore, observers perpendicular to the spin axis experience a flatter redshift profile and so see closer to the horizon.

A.2. Dependence on the Fluid Velocity

In general, the fluid will have a non-zero ϕ velocity in the ZAMO frame. In Figure 10 we show $v^{\phi'}$ for different models

from McKinney et al. (2012). We give the velocity in units of the Keplerian speed $v_K = 1/\sqrt{r}$. The "thinnermadx" models are those considered here (where the number x gives the spin),

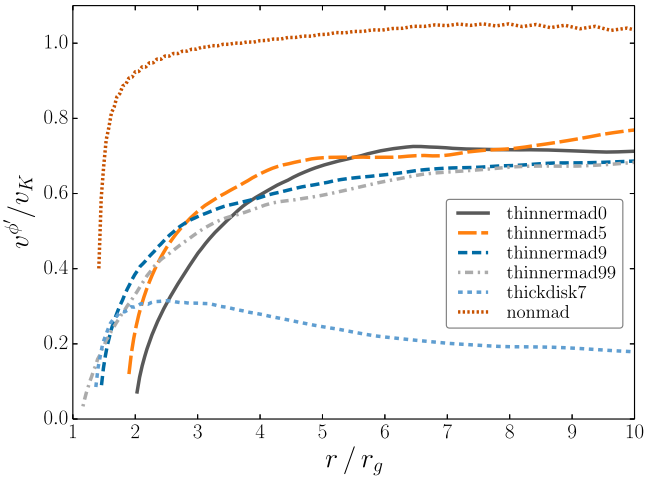

Figure 10. $v^{\phi'}$ in units of v_K for different accretion models. The SANE model is roughly Keplerian, while the MAD models are all sub-Keplerian. The velocity is approximately a constant fraction of the Keplerian speed until close to the horizon. In the lab frame, frame dragging forces the fluid to rotate with $v^{\phi} \to \Omega_H$ as $r \to r_H$.

while the "thickdisk7" and "nonmad" models are the MAD and SANE models considered in O' Riordan et al. (2016). These models have $a = 0.9375$ and $a = 0.92$, respectively. In all models, the ϕ velocity is approximately a constant fraction of the Keplerian speed until close to the horizon (where $v^{\phi'} \to 0$ since $v^{r'} \to 1$ in this frame). Motivated by this, we choose $v^{\phi'}$ to be proportional to v_K, and set $v^{\phi'} = 0$ at the horizon with a smooth transition at $r = r_{\rm ISCO}$. In Figure 11 we show the effects of varying $v^{\phi'}$ for a black hole with $a = 0.9$. The difference between the observed and comoving power is a factor of $\mathcal{R}^2$. Therefore, for photons emitted in the ϕ direction in the fluid frame, the ϕ velocity contributes to a maximum factor of ~3. Since observed photons will have a spread of $\mathcal{P}_{\phi''}$, the average difference in power will likely be much smaller than this.

To test the sensitivity of the redshift factor to the accretion model, we numerically calculate redshift profiles for the "thinnermad9," "thickdisk7," and "nonmad" models. These have similar spin, but have different velocity fields (see Figure 10 for the ϕ velocity). In Figure 12 we show the radial velocity profiles. The radial velocities are comparable in the MAD models, however, these differ significantly from the SANE case. In Figure 13 we show the redshift profiles from the different models, for observers located at $\theta = 0$ and $\theta = \pi/2$. The $\theta = \pi/2$ case should maximize potential deviations.

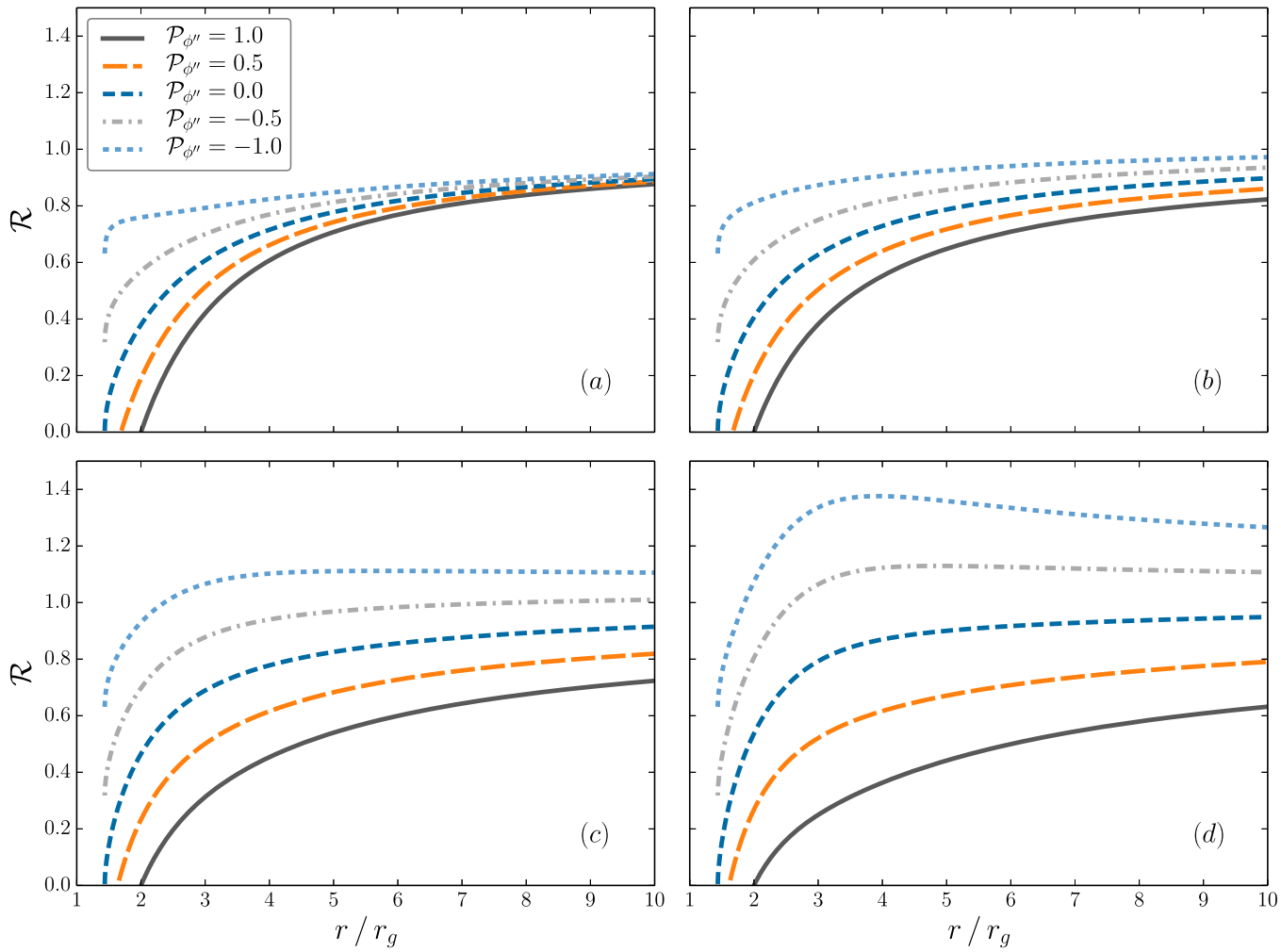

Figure 11. Redshifts for a source with $a = 0.9$, and $v^{\phi'} = \epsilon\, v_K$. We set $v^{\phi'} = 0$ at the horizon, with a transition at $r = r_{\rm ISCO}$. (a): $\epsilon = 0.0$, (b): $\epsilon = 0.2$, (c): $\epsilon = 0.6$, (d): $\epsilon = 1.0$.

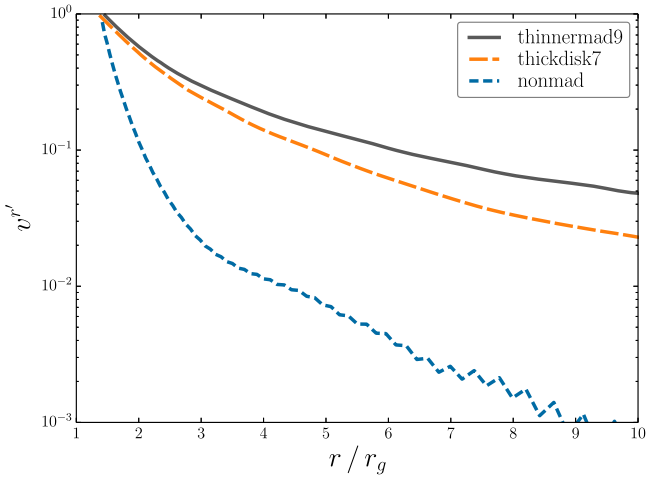

Figure 12. Radial velocity in the ZAMO frame for the MAD and SANE models with similar spin. The radial velocities are comparable in the MAD case, but the velocity profile is significantly different in the SANE case.

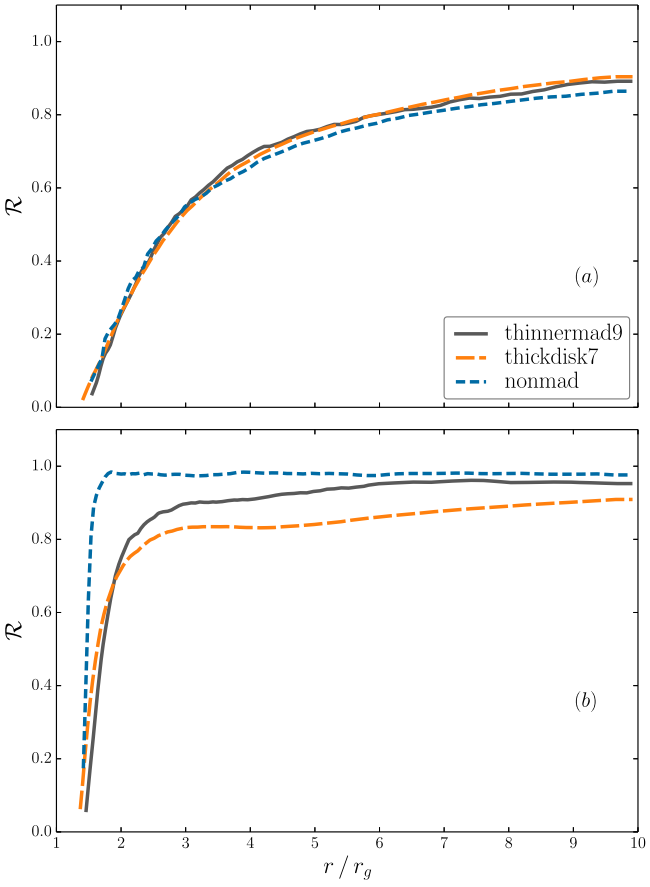

Figure 13. Redshift profiles for different accretion models. The observer is located at (a): $\theta = 0$, (b): $\theta = \pi/2$. Although these models have different velocity fields, the resulting redshift profiles are similar. In particular, for $\theta = \pi/2$ the profiles are reasonably flat until close to the horizon. Therefore, the contributions from spin and viewing angle are more important than the model-dependent fluid velocity.

Despite differences in the fluid velocity, the resulting profiles are remarkably similar. In particular, the redshift is reasonably flat until very close to the horizon. Therefore, we conclude that the model-dependent velocity contribution to the described redshift effect is minor, while the main contributions are the spin and viewing angle.

APPENDIX B
DEPENDENCE OF THE RADIATED POWER ON THE ACCRETION RATE

The GRMHD simulations are scale free. However, introducing radiation forces us to specify length, time, and mass/energy scales. The length and timescales are set by the black hole mass M. These are the gravitational radius r_g, and light-crossing time $t_g = r_g/c$. Since the fluid mass is $\ll M$, we set the mass/energy scale via the mass accretion rate

$$\dot{M} = \left| \int dA\ \rho\ u^r \right| . \tag{14}$$

For some constant μ, we can write this in terms of the Eddington rate as $\dot{M} = \mu\ \dot{M}_{\rm Edd}$. Therefore, for a fixed black hole mass, the rest mass density scales with the accretion rate as $\rho \sim \mu$. Since energy densities scale in the same sense as ρc^2, we immediately find $n \sim \mu$, $B \sim \mu^{1/2}$, and $\Theta \sim \mu^0$. The last relation follows from the fact that, for a perfect fluid, $\Theta \sim u/\rho c^2$, where u is the internal energy density. Finally, the synchrotron emissivity scales with the accretion rate as $nB^2\Theta^2 \sim \mu^2$, and the synchrotron frequency scales as $B\Theta^2 \sim \mu^{1/2}$.

REFERENCES

Ackermann, M., Anantua, R., Asano, K., et al. 2016, ApJL, 824, L20
Aharonian, F., Akhperjanian, A. G., Bazer-Bachi, A., et al. 2007, ApJL, 664, L71
Albert, J., Aliu, E., Anderhub, H., et al. 2007, ApJ, 669, 862
Aleksić, J., Antonelli, L. A., Antoranz, P., et al. 2011, ApJL, 730, L8
Avara, M. J., McKinney, J. C., & Reynolds, C. S. 2016, MNRAS, 462, 636
Bardeen, J. M., Press, W. H., & Teukolsky, S. A. 1972, ApJ, 178, 347
Belloni, T., Homan, J., Casella, P., et al. 2005, A&A, 440, 207
Blandford, R. D., & Znajek, R. L. 1977, MNRAS, 179, 433
Bosch-Ramon, V., Romero, G. E., & Paredes, J. M. 2006, A&A, 447, 263
Broderick, A. E., Johannsen, T., Loeb, A., & Psaltis, D. 2014, ApJ, 784, 7
Broderick, A. E., & Tchekhovskoy, A. 2015, ApJ, 809, 97
Cadolle Bel, M., Sizun, P., Goldwurm, A., et al. 2006, A&A, 446, 591
Cowling, T. G. 1933, MNRAS, 94, 39
Cunningham, C. T., & Bardeen, J. M. 1972, ApJL, 173, L137
Cunningham, C. T., & Bardeen, J. M. 1973, ApJ, 183, 237
Dexter, J., McKinney, J. C., & Agol, E. 2012, MNRAS, 421, 1517
Dolence, J. C., Gammie, C. F., Mościbrodzka, M., & Leung, P. K. 2009, ApJS, 184, 387
Esin, A. A., McClintock, J. E., Drake, J. J., et al. 2001, ApJ, 555, 483
Esin, A. A., McClintock, J. E., & Narayan, R. 1997, ApJ, 489, 865
Falcke, H., Körding, E., & Markoff, S. 2004, A&A, 414, 895
Fanton, C., Calvani, M., de Felice, F., & Cadez, A. 1997, PASJ, 49, 159
Fender, R. 2010, in Lecture Notes in Physics, Vol. 794 ed. T. Belloni (Berlin: Springer), 115
Fender, R. P., Belloni, T. M., & Gallo, E. 2004, MNRAS, 355, 1105
Fender, R. P., Gallo, E., & Russell, D. 2010, MNRAS, 406, 1425
Foucart, F., Chandra, M., Gammie, C. F., & Quataert, E. 2016, MNRAS, 456, 1332
Gammie, C. F., McKinney, J. C., & Tóth, G. 2003, ApJ, 589, 444
Gierlinski, M., Zdziarski, A. A., Done, C., et al. 1997, MNRAS, 288, 958
Gupta, S., Böttcher, M., & Dermer, C. D. 2006, ApJ, 644, 409
Kaiser, C. R. 2006, MNRAS, 367, 1083
Kylafis, N. D., Papadakis, I. E., Reig, P., Giannios, D., & Pooley, G. G. 2008, A&A, 489, 481
MacDonald, D., & Thorne, K. S. 1982, MNRAS, 198, 345
Magdziarz, P., & Zdziarski, A. A. 1995, MNRAS, 273, 837
Maitra, D., Markoff, S., Brocksopp, C., et al. 2009, MNRAS, 398, 1638
Markoff, S., Falcke, H., & Fender, R. 2001, A&A, 372, L25
Markoff, S., Nowak, M., Corbel, S., Fender, R., & Falcke, H. 2003, A&A, 397, 645
Markoff, S., Nowak, M. A., & Wilms, J. 2005, ApJ, 635, 1203

Markoff, S., Nowak, M. A., Gallo, E., et al. 2015, ApJ, 812, 25
McClintock, J. E., Narayan, R., Davis, S. W., et al. 2011, CQGra, 28, 114009
McKinney, J. C. 2006, MNRAS, 368, 1561
McKinney, J. C., & Gammie, C. F. 2004, ApJ, 611, 977
McKinney, J. C., Tchekhovskoy, A., & Blandford, R. D. 2012, MNRAS, 423, 3083
McKinney, J. C., Tchekhovskoy, A., & Blandford, R. D. 2013, Sci, 339, 49
Mirabel, I. F., & Rodríguez, L. F. 1994, Natur, 371, 46
Mościbrodzka, M., & Falcke, H. 2013, A&A, 559, L3
Mościbrodzka, M., Falcke, H., Shiokawa, H., & Gammie, C. F. 2014, A&A, 570, A7
Mościbrodzka, M., Gammie, C. F., Dolence, J. C., Shiokawa, H., & Leung, P. K. 2009, ApJ, 706, 497
Narayan, R., Igumenshchev, I. V., & Abramowicz, M. A. 2003, PASJ, 55, L69
Narayan, R., & McClintock, J. E. 2008, NewAR, 51, 733
Narayan, R., & McClintock, J. E. 2012, MNRAS, 419, L69
Narayan, R., Sadowski, A., Penna, R. F., & Kulkarni, A. K. 2012, MNRAS, 426, 3241
Niedźwiecki, A., Xie, F.-G., & Stępnik, A. 2014, MNRAS, 443, 1733
Niedźwiecki, A., Xie, F.-G., & Zdziarski, A. A. 2012, MNRAS, 420, 1195
O' Riordan, M., Pe'er, A., & McKinney, J. C. 2016, ApJ, 819, 95
Pe'er, A., & Casella, P. 2009, ApJ, 699, 1919
Pe'er, A., & Markoff, S. 2012, ApJ, 753, 177
Poutanen, J. 1998, in Theory of Black Hole Accretion Disks, ed. M. A. Abramowicz, G. Bjornsson, & J. E. Pringle (Cambridge: Cambridge Univ. Press)
Qiao, E., & Liu, B. F. 2015, MNRAS, 448, 1099
Remillard, R. A., & McClintock, J. E. 2006, ARA&A, 44, 49
Ressler, S. M., Tchekhovskoy, A., Quataert, E., Chandra, M., & Gammie, C. F. 2015, arXiv:1509.04717
Russell, D. M., Russell, T. D., Miller-Jones, J. C. A., et al. 2013, ApJL, 768, L35
Rybicki, G. B., & Lightman, A. P. 1979, Radiative Processes in Astrophysics (New York: Interscience)
Sądowski, A., Narayan, R., Tchekhovskoy, A., et al. 2015, MNRAS, 447, 49
Sironi, L., & Spitkovsky, A. 2014, ApJL, 783, L21
Tchekhovskoy, A., & McKinney, J. C. 2012, MNRAS, 423, L55
Tchekhovskoy, A., McKinney, J. C., & Narayan, R. 2012, JPhCS, 372, 012040
Tchekhovskoy, A., Narayan, R., & McKinney, J. C. 2010, ApJ, 711, 50
Tchekhovskoy, A., Narayan, R., & McKinney, J. C. 2011, MNRAS, 418, L79
Titarchuk, L. 1994, ApJ, 434, 570
Yuan, F., & Narayan, R. 2014, ARA&A, 52, 529
Yuan, F., Zdziarski, A. A., Xue, Y., & Wu, X.-B. 2007, ApJ, 659, 541